Possible coexistence of magnetism and paramagnetic singularity in lightly Fe-doped WTe_2

Dinesh Baral,[1,2,*] Rabindra Basnet,[3,4,*] William R. Scougale,[1] Raz Q. Rivlis,[1] Dinesh Upreti,[3] Yuri Dahnovsky,[1] Jin Hu,[2,3,†] and TeYu Chien[1,5,‡]

[1]*Department of Physics & Astronomy, University of Wyoming, Laramie, Wyoming 82071, USA*
[2]*Institute for Nanoscience and Engineering, University of Arkansas, Fayetteville, Arkansas 72701, USA*
[3]*Department of Physics, University of Arkansas, Fayetteville, Arkansas 72701, USA*
[4]*Department of Chemistry and Physics, University of Arkansas at Pine Bluff, Arkansas 71603, USA*
[5]*Center for Quantum Information Science & Engineering, University of Wyoming, Laramie, Wyoming 82071, USA*

(Received 28 September 2023; revised 14 December 2023; accepted 4 June 2024; published 17 June 2024)

Topological semimetals possess nodal or nodal-line phases where conduction and valence bands touch at points or lines in momentum space, respectively. Such band touching is symmetry protected and gives rise to exotic and interesting electronic properties. Coupling topological order with magnetism provides a platform for exploring time-reversal (TR) symmetry breaking topological physics, such as axion electrodynamics, inverse spin-galvanic effect, and the quantized anomalous Hall effect. The Weyl semimetal (WSM) requires breaking either TR symmetry or lattice inversion symmetry (I). By doping inversion-symmetry-broken WSM with magnetic dopants, one can expect to create a WSM with both symmetries breaking simultaneously. Here, structural, electrical, and magnetic properties of $Fe_xW_{1-x}Te_2$ ($x = 0$ and 0.011) are reported. It is revealed that, with a small Fe doping concentration ($x = 0.011$), a ferromagnetism is induced at low temperature (<10 K). Scanning tunneling microscopy and spectroscopy measurements in $Fe_{0.011}W_{0.989}Te_2$ further reveal only substitution and no intercalated dopants being observed. The probabilities of the Fe substitutions at the two nonequivalent W sites are quantified with equal probability. The dI/dV point spectra indicates that the Fe substitution in WTe_2 manifests itself as electron doping regardless of doping sites. The results clearly reveal the possible coexistence of magnetism and Weyl points in the lightly Fe doped WTe_2 at low temperature. This provides an ideal system for further study on the interplay between the topological Weyl points and the TR symmetry breaking.

DOI: 10.1103/PhysRevB.109.245419

I. INTRODUCTION

Ever since the realization of the topological insulators [1–5], inducing magnetism in topological phases has been widely pursued [6–15] for understanding the influence of the time-reversal (TR) symmetry breaking on the topological phases. Phenomena, such as axion electrodynamics [8,10], inverse spin-galvanic effect [9], quantized anomalous Hall effect [11], enhanced anomalous Hall effect [16], magnetically tunable point nodes [17], and emergent domain wall properties [18], have been reported in such systems. The Weyl semimetals (WSM) requires the breaking of either the TR symmetry or the lattice inversion symmetry (I). This leads to signatures in the band structures of WSM where conduction and valence bands touch to form pairs of nodes with opposite chirality at different points in three-dimensional (3D) momentum space. A number of magnetic WSM have been proposed and demonstrated, such as $Y_2Ir_2O_7$ [19], $HgCr_2Se_4$ [20], $Co_3Sn_2S_2$ [21], and certain Co_2-based Heusler compounds [22–24]. Breaking both TR and I is expected to be unfavorable for the Weyl phase from a theoretical perspective [25]. Discovering how the Weyl phase is suppressed or possibly survives by breaking both symmetries owing to some intrinsic or extrinsic reason, would be important for better understanding of this topological phase and would help to explore other exotic phenomena such as large anomalous Hall conductivity and large anomalous Hall angle [26,27].

Transition metal dichalcogenides (TMDs) are layered materials with van der Waals (vdW) forces between the layers and exhibit thickness-dependent electrical and optical properties when approaching monolayer thickness [28]. These TMDs are hosts of both electronic correlations and novel magnetisms, which are the sources of many exotic phenomena, such as Mott physics [29,30], charge density waves [31], superconductivity [32–34], and large magnetoresistance [35,36]. These properties lead to variety of potential applications, such as the catalysis of chemical reactions [37], solid-state lubricants [38], next-generation electronics [39–41], optoelectronics [42,43], flexible electronics [44], and transparent electronics [45,46]. WTe_2 is an unusual material, where topology, correlations and spin-orbit coupling are all simultaneously important [47–49], leading to various interesting properties, such as excitonic insulating observed in monolayer WTe_2 [50], extremely large positive magnetoresistance [35], electric-field switchable Berry curvature dipole [51], in-plane interlayer sliding crystal phase switching [52], type-II Weyl semimetal phase [53–55], charge ordering [56] and 2D

*These authors contributed equally to this work.
†Contact author: jinhu@uark.edu
‡Contact author: tchien@uwyo.edu

topological insulator [47,57] with the nontrivial edge states [48,56,58,59] that supports the quantum spin Hall effect in the monolayer form. Since the topological Weyl semimetal and 2D topological insulator phases are sensitive to TR symmetry, using magnetic dopants to induce magnetism in WTe_2 would offer opportunities for further investigating the exotic topological phases and possibly opens novel pathway for topological fermion-based electronics and spintronics.

Doping TMDs with magnetic elements has been reported to induce local magnetic moment [60–62], such as Fe doping in SnS_2 [62,63], and MoS_2 [64]; Mn doping in MoS_2 [64,65], $MoSe_2$ [66], $MoTe_2$ [66], and WS_2 [66]**;** as well as Co doping in MoS_2 [64]. Even near-room temperature ferromagnetism has been reported in Cr-doped WTe_2 [60] and Fe-doped ZrS_2 [61]. Interestingly, diluted magnetic doping (less than 6%) is sufficient to establish ferromagnetic (FM) ordering on TMDs [60–62]. It is still elusive but critical to know that if the topological phases still exist with the induced magnetism in these materials. Here, we aim to break TR symmetry in a broken-I symmetry WSM − WTe_2 through doping magnetic element, Fe. Particularly, the magnetization induced with a small Fe substitutional doping level (1.1%) in WTe_2 and the signs of the coexistence with the Weyl points are identified.

II. METHODS

Sample Preparation, EDS, XRD, and Hall Measurements. Single crystal $Fe_xW_{1-x}Te_2$ were grown by a two-step method. First, a polycrystalline precursor was prepared by heating the stoichiometric mixture of W, Fe, and Te at 700 °C for two days. The precursor was then used as a source for chemical vapor transport (CVT) growth with a temperature gradient from 900 °C to 800 °C for two weeks using I_2 as the transport agent to obtain millimeter sized single crystal. The compositions of the obtained crystals were determined by energy-dispersive x-ray spectroscopy (EDS). The crystal structure has been examined using x-ray photoemission (XRD) to confirm the crystallinity of the sample. Magnetization measurements were performed in a magnetic property measurement system (MPMS3 superconducting quantum interference device (SQUID), Quantum Design). Hall effect was measured using a physical property measurement system (PPMS, Quantum Design).

STM Measurement. For low temperature scanning tunneling microscopy (STM) (Scienta Omicron LTSTM) measurements, a $Fe_xW_{1-x}Te_2$ single crystal was attached onto a stainless-steel sample plate using a conductive epoxy (EJ2312, from Epoxy Technology). Samples were then cleaved in UHV (base pressure: 1.5×10^{-10} mbar) at room temperature prior to the STM measurements. The STM/S results presented here were measured at 77 K with a base pressure of 6.3×10^{-12} mbar. A chemically etched W tip was used for STM/S measurements. Differential conductance (dI/dV) were measured with lock-in technique using the modulation frequency of 5.577 kHz and modulation voltage of 20 mV. The STM images were analyzed using WSxM [67].

Simulation of Topographic Images. Density functional theory (DFT) calculations were performed using the Vienna ab initio Simulation Package (VASP) [68–70] based on the projector augmented wave method [71]. The Perdue-Burke -Ernzerhof version [72] of the generalized gradient approximation was used in the calculation. The plane wave energy cutoff was set to 500 eV. The energies were converged to 10^{-4} eV. The initial ionic relaxation for the bulk crystal was performed using $19 \times 11 \times 7$ k-point sampling in the Brillouin zone and the energies were converged to 10^{-6} eV. The surface calculations were performed using a $3 \times 3 \times 1$ supercell of bilayer WTe_2 with $12 \times 8 \times 1$ k-point sampling in the Brillouin zone. A vacuum layer of ∼15 Å was used between the slabs. Van der Waals interactions were accounted for using the DFT-D3 correction method adopted from Grimme *et al.* [73] The simulated STM images were generated using VASP [68–71] by integrating density of states from E_F to $E_F + 0.3$ eV to compare with the experimental STM images obtained at the same bias-voltage. The total energies of Fe substituted WTe_2 and of pristine WTe_2 were also calculated using VASP.

III. RESULTS AND DISCUSSIONS

WTe_2 is a vdW material formed by stacking Te-W-Te sandwich layers [74,75] [Figs. 1(a) and 1(b)]. Bulk WTe_2 crystallizes with the space group $Pmn2_1$ and the lattice constants of $a = 3.496$ Å, $b = 6.282$ Å, and $c = 14.07$ Å [76,77]. The crystal in its pristine phase has two nonequivalent top-layer Te and W sites as shown in Fig. 1(b), marked by Te_1, Te_2 and W_1, W_2, respectively. Te_1 and Te_2 on the top surfaces are responsible for the observed features in STM images in most scanning conditions [77]. Te_2 is positioned slightly higher compared with Te_1 along the c direction. Both the pristine and Fe doped WTe_2 single crystals used in this work were grown by a chemical vapor transport method (see Methods). The composition analysis was achieved through counting the observed number of dopants per area in STM images as will be discussed below to be 1.1%. The EDS yielded negligible Fe peaks making it unreliable for determining the doping level. The lattice structures were examined by XRD. Figures 1(c) and 1(d) show the (00L) XRD peaks of pristine and 1.1% Fe doped WTe_2 samples. Close examination of the diffraction peak (002) of pristine and 1.1% Fe doped WTe_2 shows a peak shift towards a higher angle upon doping as shown in Fig. 1(d), suggesting a decrease in interplanar spacing. Providing a smaller ionic radius of Fe compared to W, such a reduction implies a scenario of substitution doping at this doping level, rather than intercalation doping which generally expands the interlayer spacing.

The effect of Fe doping on magnetism was characterized by magnetization measurements, as shown in Fig. 2. A quartz sample holder was used for the measurements to minimize the contribution of the sample holder, and consequently the magnetic field was applied parallel to the sample cleavage plane (i.e, the ab plane). The contribution from the sample holder was removed from the measured data to obtain the magnetic properties of the samples. To ensure accuracy, the measurements on pristine and Fe doped samples were performed on the identical sample holder at the same temperatures. As shown in Figs. 2(a) and 2(b), despite displaying an overall diamagnetic response [upper insets of Figs. 2(a) and 2(b)], both WTe_2 and $Fe_{0.011}W_{0.989}Te_2$ exhibit a field-induced polarization behavior characterized by a strong nonlinear

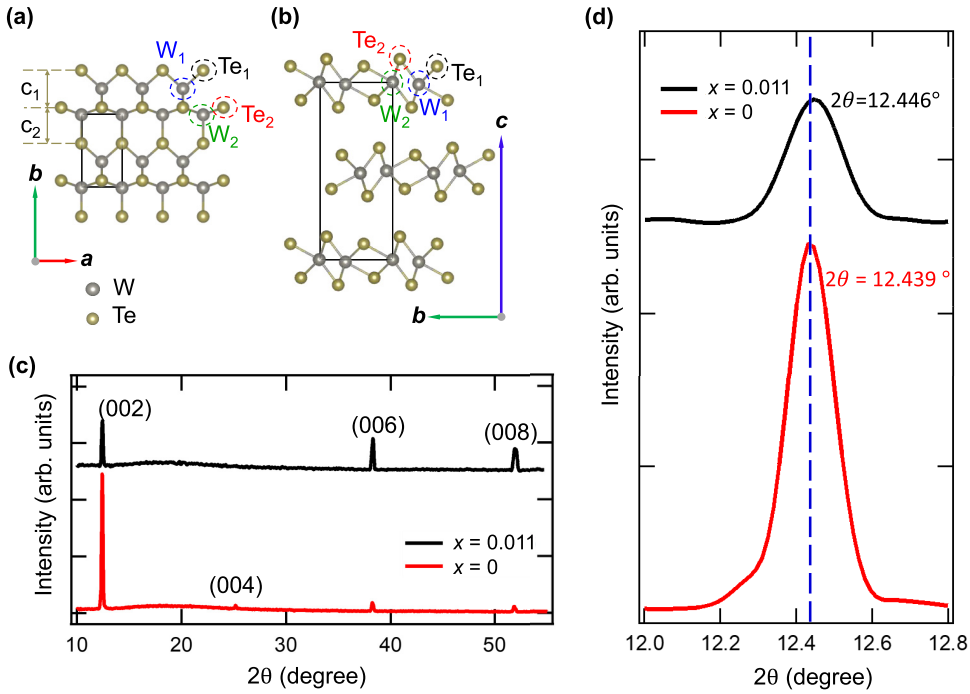

FIG. 1. Crystal structure of $Fe_xW_{1-x}Te_2$. (a) Top view of WTe_2 crystal structure showing the top Te layer and the W layer. The bottom Te is hidden in this drawing. (b) Side view of WTe_2 crystal structure showing three Te-W-Te layers. The unit cells are marked by solid rectangular boxes in both (a) and (b). Te_1 and Te_2 represent the nonequivalent Te sites; and W_1 and W_2 represent the nonequivalent W sites in the crystal. (c) XRD of the pristine and $Fe_{0.011}W_{0.989}Te_2$ show narrow peaks which indicates high quality single crystals. (d) Comparison of XRD (002) peak positions of the pristine and the 1.1 % Fe doped WTe_2. Peak positions are obtained from Gaussian fitting.

field dependence near zero field. Such polarization behavior occurring from 2 to 300 K can be clearly seen after removing the diamagnetic background [Figs. 2(a) and 2(b), main panel]. Accompanied with the polarization is the hysteresis loops, as shown in the lower insets in Figs. 2(a) and 2(b), from which the remanent magnetization at zero field and coercivity from 2 to 300 K are extracted as shown in Fig. 2(e). All those observations appear consistent with ferromagnetic behavior.

The low field nonlinear magnetization for WTe_2 has been previously reported to be attributed to defect-induced weak ferromagnetism [60]. In our WTe_2 single crystals, we indeed observed a very tiny amount of Te vacancies in STM experiments as discussed later. However, such trace amount of Te vacancies can hardly explain the substantial nonlinear magnetization seen in Fig. 2(a). As will be shown below, the observed temperature dependence of magnetic properties is also hardly attributed to a vacancy-induced magnetism. In fact, such a magnetization anomaly is more likely arising from the spin singularity at the Weyl point. This phenomenon was observed in topological insulators [78,79] in which each individual gapless surface Dirac cone exhibits opposite spin helicities for the upper and lower half of the Dirac cone. Such spin texture leaves a singularity at the Dirac point, causing the spins of the corresponding Dirac fermions to orient randomly at zero field but align with even a small magnetic field. Therefore, this paramagnetic response of Dirac fermions at the Dirac point causes a low field polarizationlike feature in magnetization measurements, which manifest into a cusp-like feature centered at zero field in differential susceptibility dM/dH. Because this Dirac paramagnetic singularity arises from the spin singularity at the Dirac point and thus should be temperature-independent, robust susceptibility cusp against temperature variation is considered as the evidence for the presence of such paramagnetic singularity [78,79].

In addition to topological insulators, paramagnetic singularity has also been observed in topological semimetals due to the bulk Dirac cones [80,81]. In Weyl semimetals such as WTe_2, the lift of spin degeneracy causes the emergence of a pair of Weyl cones with opposite chirality. For each of the Weyl cones, the opposite spin textures above and below the Weyl point are expected to give rise to a similar singularity. Indeed, as shown in Fig. 2(c), differential susceptibility $dM/d(\mu_0 Hd)$ for WTe_2 is essentially temperature-independent from 2 to 300 K. Vacancy-induced ferromagnetism has been reported to persist up to room temperature [82], but it weakens with increasing temperature [82]. Therefore, the observed anomaly in magnetism in pristine WTe_2 is most likely governed by paramagnetic singularity for Weyl points.

For the Fe-doped samples, Fe-induced magnetism starts to play a substantial role in mediating magnetization. Figure 2(d) displays the differential susceptibility at zero field for the $x = 0.011$ sample. Differential susceptibility at 2 K is well above other temperatures, which, as will be shown below, is caused by the Fe-induced magnetism. In contrast, differential susceptibilities measured above 20 K almost overlap, which is consistent with the temperature-independent nature of paramagnetic singularity. Figure 2(f) summarizes the temperature dependence of differential susceptibilities for the pristine WTe_2 and the $x = 0.011$ samples. The temperature

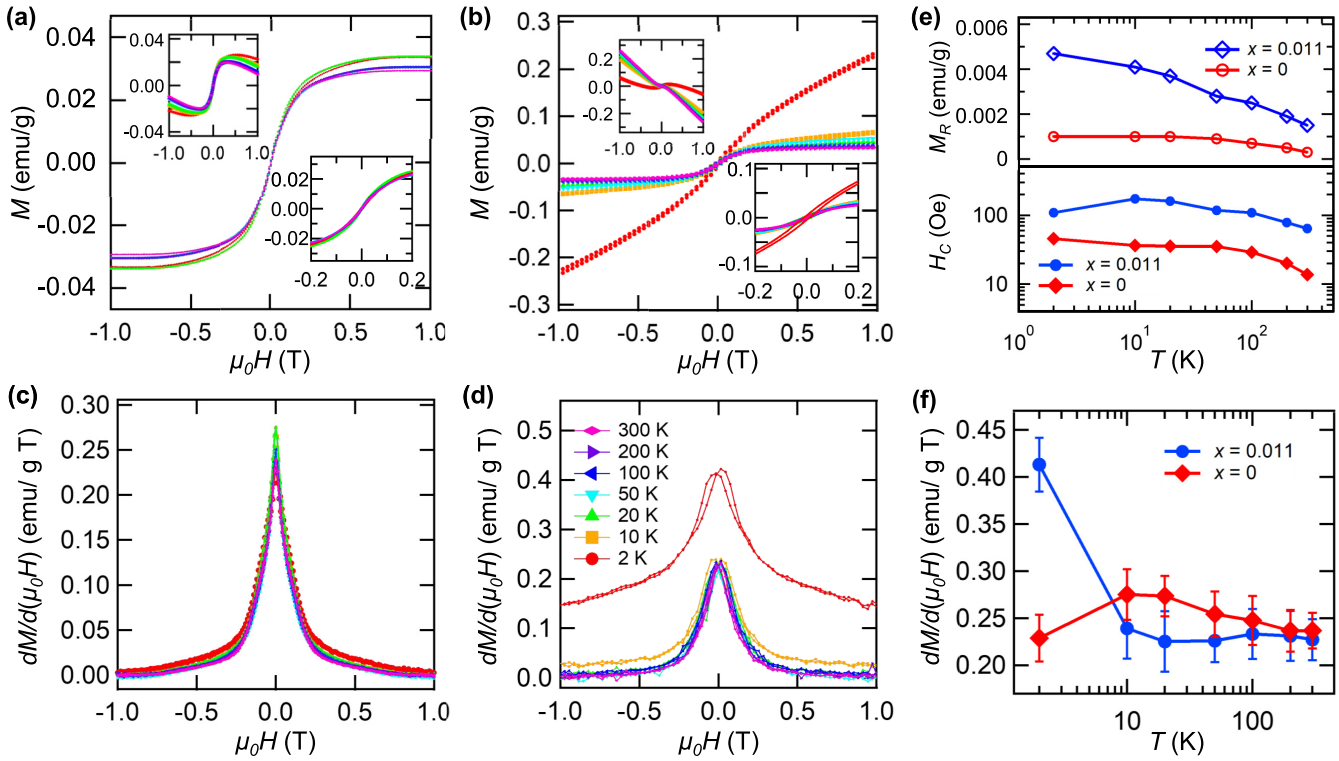

FIG. 2. Magnetic properties of $Fe_xW_{1-x}Te_2$, ($x = 0$ and 0.011). (a) and (b) M vs μ_0H measurements of x = 0 (a) and x = 0.011 (b) at various temperatures ranging from 2 to 300 K with B ∥ a-b plane. Inset: Upper inset in both (a) and (b) shows the raw data before removing the diamagnetic background. Lower inset in both (a) and (b) is the zoom-in plot of the low-field range between -0.2 T and +0.2 T, to highlight the presence of hysteresis loop. (c) and (d) Differential magnetic susceptibility [$dM/d(\mu_0H)$] obtained from the data shown in (a) and (b), respectively. Legend in (d) applies to all figures from (a) through (d). In (d), differential magnetic susceptibility at 2 K for the $x = 0.011$ sample is higher than that of measurements at other temperatures. This is due to its strong magnetization nonlinearity covering a relatively broader field region at 2 K. At high field, differential magnetic susceptibility at various temperatures overlaps. (e) Upper panel: Remanent Magnetization (M_R) and lower panel: Coercivity (H_C) vs T, obtained from (a) and (b). (f) Maximum differential magnetic susceptibility vs T, obtained from (c) and (d).

variation of differential susceptibility for the pristine WTe_2 is rather weak and is attributed to paramagnetic singularity as discussed above. For the $x = 0.011$ sample, differential susceptibility is essentially temperature independent above 20 K, but increases rapidly upon lowering temperatures below 20 K and reaches a maximum value of 0.45 emu/g T at T = 2 K. The absence of obvious temperature dependence at high temperatures can be ascribed to the paramagnetic singularity for Weyl points similar to that in pristine WTe_2. Below 20 K, however, the strong increase of susceptibility is most likely caused by the rise of ferromagnetism due to Fe doping. As will be discussed below, Fe doping likely induces short-range ferromagnetic correlations, which manifest into the growth of susceptibility with reducing temperature.

Therefore, the temperature dependence for the zero-field differential susceptibility in Fe-doped WTe_2 can be understood in terms of the coexistence of paramagnetic singularity for Weyl points and ferromagnetism from Fe doping. As shown in Fig. 2(e), remanent magnetization and coercivity of the magnetic hysteresis loop for the lightly Fe-doped sample are stronger than that of the pristine WTe_2, implying the presence of Fe-induced magnetism. The gradual suppression of hysteresis loop with rising temperature is also consistent with such a scenario. However, differential susceptibility dM/dH is expected to reduce at higher temperatures for the case of magnetism. Hence, the observed temperature-independent differential susceptibility in a lightly Fe-doped sample should be attributed to the coexistence of paramagnetic singularity and ferromagnetism. As shown in Fig. 2(f), at low temperatures (below 20 K), short-range ferromagnetic correlations dominate the strong increase of differential susceptibility. When magnetism is strongly suppressed above 20 K, the temperature-independent paramagnetic singularity becomes significant, and differential susceptibility is comparable with that of the pristine WTe_2. This result indicates possible coexistence of ferromagnetism caused by Fe doping and the Weyl points. How does the Weyl state persists upon breaking both time reversal and inversion symmetries, and whether the observed coexistence is due to phase separation or not, need further investigation.

With the above picture of ferromagnetism induced by Fe-doping, next we clarify the microscopic mechanism of the rise of ferromagnetism. Doping in TMDs can be categorized into surface adsorptions [83,84], intercalation [85,86], and substitutions [87–90]. The Fe dopants in this work are incorporated into the WTe_2 crystals during the synthesis. Thus, the surface adsorptions are not in consideration here. Both intercalation and substitution have been observed in Fe-doped TMD, such

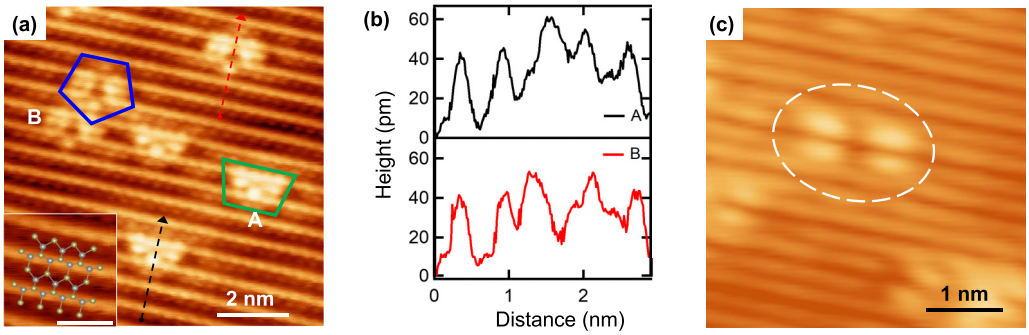

FIG. 3. STM topographic image: (a) Atomic resolution image showing the two distinct types of defects: A (green box) and B (blue box). Inset: crystal structure overlaid on the STM image of the defect-free region. Scale: 1 nm. (b) Line profile across the black and red arrows in (a). (c) Te vacancy defects. Scanning condition of (a) and (c) : $U = 200$ mV, $I_{\rm set} = 500$ pA.

as Fe-substituted SnS_2 [62] and ZrS_2 [61], and Fe-intercalated TaS_2 [91] and NbS_2 [91]. As discussed above (Fig. 1), the shrinking of interlayer spacing of the Fe-doped WTe_2 implies the substitution of W by smaller Fe ions. Fe substitution in the lightly doped samples is further demonstrated and confirmed by STM experiments and DFT calculations. To investigate the doping nature of the Fe dopants in WTe_2, STM/S is utilized. Since Te_2 is located higher compared to Te_1, it usually appears as brighter feature in the STM topographic image [77]. In the crystal structure shown in Fig. 1(a), the distances between $Te_2 - Te_1$ rows are marked as c_1 (3.19 Å) and c_2 (3.09 Å). Using the differences between c_1 and c_2, the crystal orientation in the STM images was determined and is later compared with DFT simulated topographic images. There are two dominant defect types which are illustrated and labeled as A and B shown in Fig. 3(a). Typical defects in TMDs could be vacancy defects due to missing atoms [58]. When dopants are involved, intercalations [85,86] and substitutions [87–90,92] are expected as well. The STM images with the vacancy defects were previously reported [93,94] and have distinctly different appearances when compared with the defect images as shown in Fig. 3(a). Very few vacancy defects have been observed with similar appearances as previously reported [93–95] and shown in Fig. 3(c), demonstrating that the crystal is of high quality. Intercalation of Fe between the layers is also ruled out, based on the STM topography. It is expected that the intercalated dopants appeared in STM topographic images as laterally diffused protrusions with lateral sizes in few nm scale, and without interrupting the surface crystal structure [86,96]. The images of the defects shown in Figs. 3(a) and the line profiles of the topography near the defects shown in 3(b) exhibit clear local density of state reconstruction, and atomic scale lateral dimensions, which are contrary to the expected appearances for the intercalated dopants. Thus, it is believed that these observed defects are the substitutions of Fe at W sites in $Fe_{0.011}W_{0.989}Te_2$. As already discussed, WTe_2 has two nonequivalent W sites, W_1 and W_2, as shown in Figs. 1(a) and 1(b). The A and B defect types observed are suspected to be Fe substitutions at the two nonequivalent W sites.

To confirm that the Fe substitutions of the two nonequivalent W sites are responsible for the A and B defect types, simulated STM images of the Fe substituted WTe_2 are performed. Regions far away from the doped sites, such as that shown in Fig. 4(a), agree well with the reported lattice structure of the pristine WTe_2. The brighter and the dimmer chains in the STM topography [Figs. 4(a)–4(c)] and in the simulated images [Figs. 4(d)–5(f)] correspond to the Te_2 and Te_1 rows, respectively. The distances between the Te_1 and Te_2 rows [c_1 and c_2 shown in Fig. 4(a)] are used to unambiguously determine the crystal orientations of the STM images. Figures 4(b) and 4(c) shows the magnified atomic resolution images of the defect types A and B, respectively. The simulated STM images for the Fe substitutions at the two nonequivalent W sites, namely W_1 and W_2, are shown in Figs. 4(e) and 4(f), respectively. By comparing the features observed in the experimental and the simulated STM images, the doping sites, A and B, are assigned to the Fe substitutions at W_1 and W_2 sites, respectively. Furthermore, nine distinct STM topographic images were analyzed to investigate the preferential doping site and to determine the doping level. Figure 5 shows an example of such topographic image. Bright spots in Fig. 5(a) are the doping sites presenting concentration of Fe substitution on WTe_2. A total of 317 dopants (Fe) were identified in a total surface area equivalent to 14 246 unit cells of WTe_2. This indicates that 1.1% ($= \frac{N_A+N_B}{\rho_W \times N_{\rm cell}} = \frac{317}{2 \times 14246}$) of W atoms are substituted by Fe atoms, where N_A and N_B are number of A and B defects, respectively, in the total number of unit cells ($N_{\rm cell}$); ρ_W is the number of W per unit cell. In the magnified images [Fig. 5(b)], two different types of doped sites can be distinguished easily. These images were taken at random locations of the sample, and it was observed that type A and B are randomly distributed with no preferential sites. It is revealed that there are 150 A sites and 167 B sites identified, indicating that the probabilities of the Fe substitution doping at W_1 and at W_2 sites are 47% and 53%, respectively.

The similar probabilities of the two substitution doping sites, A and B, agree well with the calculated formation energies. The formation energy, $E_{\rm form}$, of the Fe substitution doping is defined [88,95] as

$$E_{\rm form} = E_{\rm tot,sc}[{\rm FeWTe_2}] - E_{\rm tot,sc}[{\rm WTe_2}] + \mu[{\rm W}] - \mu[{\rm Fe}]. \quad (1)$$

The evaluations of the formation energy can be achieved by the following procedures.

(a) $E_{\rm tot,sc}[{\rm FeWTe_2}]$ is the total energy of the $3 \times 3 \times 1$ supercell of bilayer WTe_2 with one Fe substitution at a certain W site (W_1 or W_2). Values of these quantities are

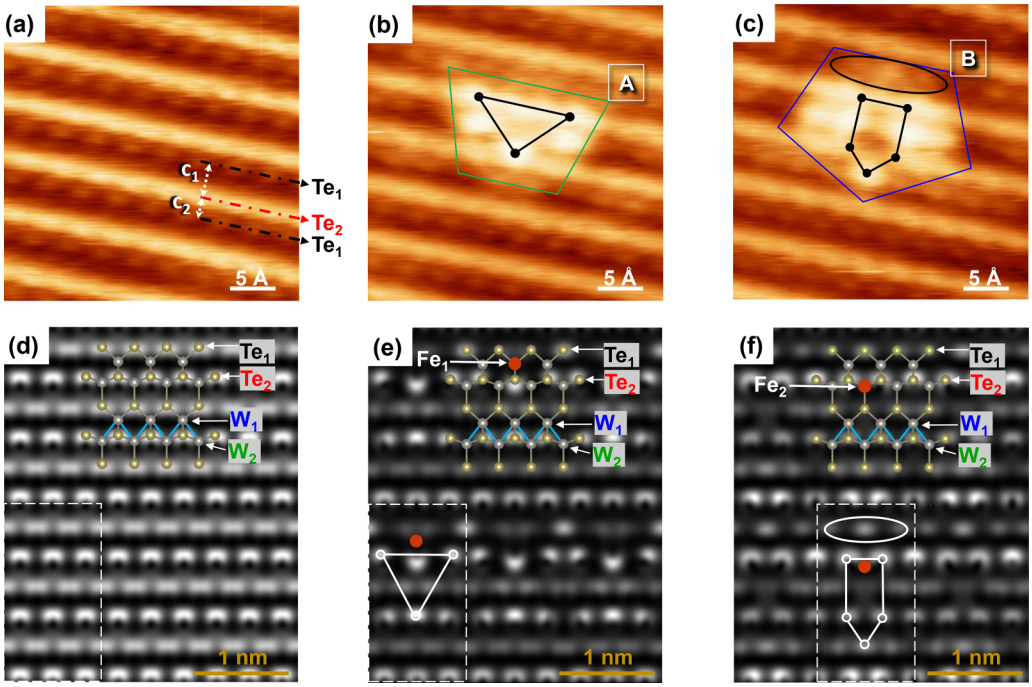

FIG. 4. Experimental and simulated STM images of $Fe_{0.011}W_{0.989}Te_2$. Experimental STM topographic images of the (a) pristine WTe_2 (far from the defects); (b) type A; and (c) type B doped sites. Scanning condition: $U = 300$ mV, $I_{set} = 1$ nA. The simulated STM images of the (d) pristine WTe_2; (e) W_1 substitution site; and (f) W_2 substitution site. Dashed boxes represent the 3×3 supercells of the bilayer WTe_2 used in the simulation. Crystal structure of the top Te-W layer [Fig. 1(a)] is overlaid for showing the substitution sites in the simulated STM images.

obtained from VASP [69–71]: $E_{tot,sc}[FeWTe_2] = -699.5984$ eV and -699.6014 eV for Fe substituting W_1 and W_2 atoms, respectively.

(b) $E_{tot,sc}[WTe_2]$ is the total energy of $3 \times 3 \times 1$ supercell of pristine bilayer WTe_2 and is calculated to be -704.6918 eV.

(c) $\mu[W]$ is the chemical potential of W in the pristine WTe_2 and is determined using the relation: $\mu[WTe_2] = \mu[W] + 2\mu[Te]$, where $\mu[WTe_2]$ is the chemical potential of WTe_2 in a pristine crystal. $\mu[WTe_2]$ equals to the total energy per formula unit of WTe_2, $E_{tot,fu}[WTe_2]$. As the unit cell of WTe_2 contains four formula units of WTe_2 [as shown in Figs. 1(a) and 1(b)], $E_{tot,fu}[WTe_2]$ equals to 1/4 of the total energy of WTe_2 unit cell, $E_{tot,uc}[WTe_2]$. Thus,

(i) $E_{tot,fu}[WTe_2] = \frac{1}{4} \times E_{tot,uc}[WTe_2] = -22.1106$ eV.

(ii) $\mu[Te]$ is the chemical potential of Te in its natural form so it equals to the total energy per Te atom in the crystal. Te crystallizes in trigonal structure having three Te atoms in the unit cell. Thus, $\mu[Te]$ can be determined as 1/3 of total energy of the unit cell of Te, $E_{tot,uc}[Te]$. That is, $\mu[Te] = \frac{1}{3} \times E_{tot,uc}[Te] = -3.1423$ eV.

Putting these together, one can get $\mu[W] = E_{tot,fu}[WTe_2] - 2\mu[Te] = -15.8260$ eV.

(d) $\mu[Fe]$ is the chemical potential of Fe in its natural form so it can be determined as the total energy per Fe atom in the crystal, i.e., body centered cubic (bcc). As the bcc crystal of Fe contains two Fe atoms per unit cell, $\mu[Fe]$ equals to 1/2 of the total energy of the unit cell of Fe, $E_{tot,uc}[Fe]$. So, $\mu[Fe] = \frac{1}{2} \times E_{tot,uc}[Fe] = -8.2249$ eV.

Putting these values together into Eq. (1), one would obtain the formation energies of the Fe substitutions at W_1 and W_2 sites to be -2.5077 eV and -2.5107 eV, respectively. The negative formation energies indicate that the Fe substitutions are stable. The difference in the formation energies between the two substituting sites, W_1 and W_2, is merely 3 meV. This small difference in the formation energies suggests that the substitution in both sites should be equally probable, which is consistent with the experimental results.

Magnetism induced by low Fe doping has been observed in a few layered materials such as SnS_2 [62] and ZrS_2 [61]. When a small amount of Fe is present in TMDs, the magnetic ordering should be short-range in nature. A recent theoretical work predicts that weak long-range FM interactions in monolayer $MoTe_2$ can occur at 15% of Fe atomic

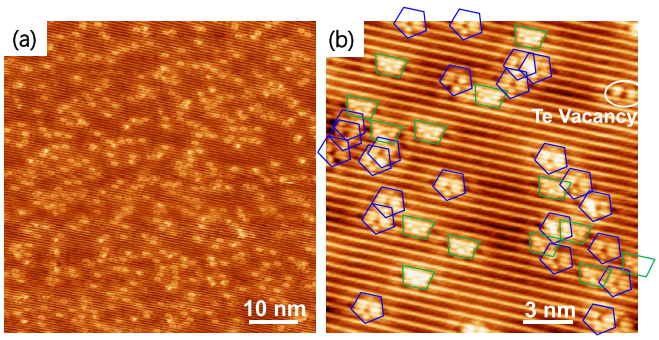

FIG. 5. Density of W substitution sites. (a) STM topographic image of the 50×50 nm^2 surface of $Fe_{0.011}W_{0.989}Te_2$. (b) STM topographic image of 15×15 nm^2 surface showing two different doped sites, namely A (green) and B (blue). Scanning condition: $U = 200$ mV, $I_{set} = 0.5$ nA.

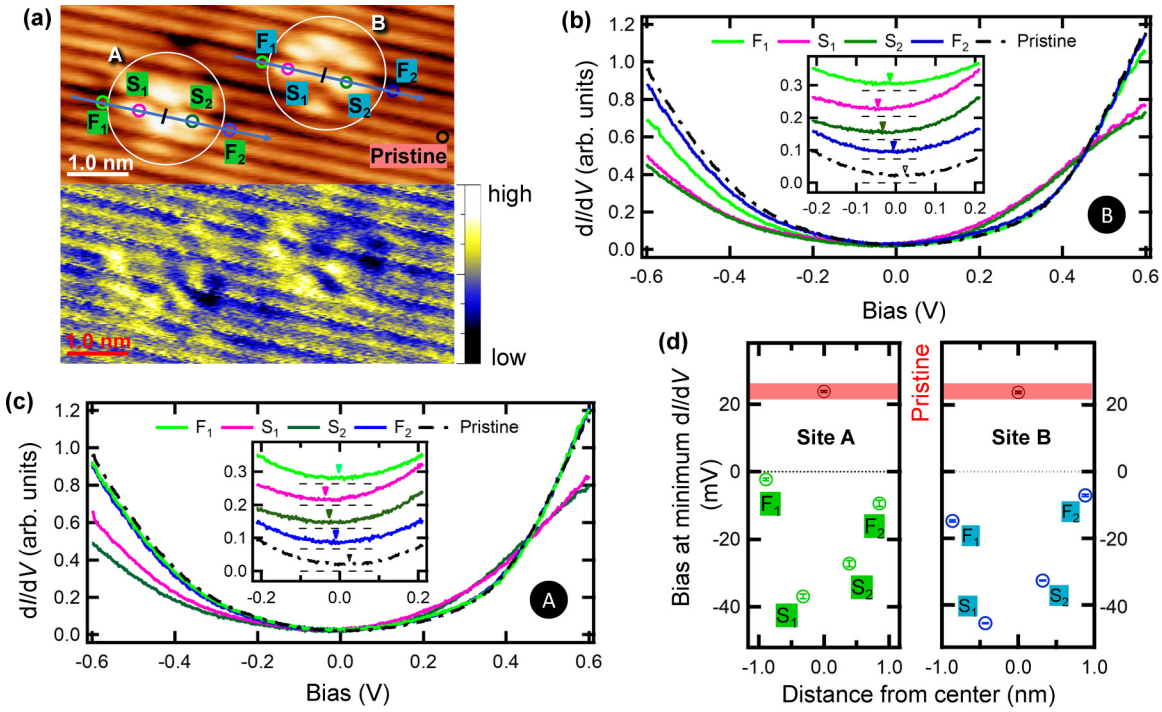

FIG. 6. Electron doping with Fe dopants. (a) STM topography (top panel) and *dI/dV* mapping (bottom panel) of a region showing both the substitution sites A and B. Scanning condition: $U = 200$ mV, $I_{set} = 0.5$ nA. Locations of the spectra shown in (b) and (c) are indicated here. (b) and (c) *dI/dV* spectra measured near the substitution site B, and A, respectively. Inset: zoomed in view of the *dI/dV* near Fermi energy. Each spectrum in the inset is shifted vertically for better comparison. The horizontal dashed lines indicate the zero level of the corresponding spectrum. (d) Spectrum minimum biases of the *dI/dV* spectra are summarized.

substitution [97]. Indeed, in the $x = 0.011$ sample, the STM results (Fig. 5) have revealed a large average distance between Fe atoms, over which magnetic exchange coupling can hardly occur. A Kondo or a Ruderman-Kittel-Kasuya-Yosida like exchange coupling between Fe local moments may occur through itinerant electrons. Therefore, Fe-induced ferromagnetism is expected to be tunable by carrier density and the amount of Fe dopant, which paves a way to investigate the interplay between the Type-II Weyl state and the magnetism in WTe_2. As discussed above, the temperature dependence of differential susceptibility [Figs. 2(c) and 2(d)] implies the paramagnetic singularity from Weyl points persists in the 1.1% Fe-substituted sample, suggesting the coexistence of the Weyl state and magnetism. Therefore, combined with the layered structure of WTe_2, the findings in this work could further provide insights into Weyl-fermion based electronics and spintronics.

To understand the differences of the impacts of the substitution sites on the electronic properties, the *dI/dV* point spectra are taken at the vicinity of both types of the substitution sites, namely A and B. *dI/dV* spectra taken on the site B and A are shown in Figs. 6(b) and 6(c), respectively. *dI/dV* spectra were taken at symmetric points [sides (S_1 and S_2) and far (F_1 and F_2)] on site A (W_1 substitution) and site B (W_2 substitution) as labeled in Fig. 6(a). For comparison, the *dI/dV* spectrum taken at locations far from the doping sites is also plotted as "pristine". Each spectrum presented in Figs. 6(b) and 6(c)) is averaged over 5 to 10 spectra taken at the same location. It is obvious that the spectra taken at F_1 and F_2 are similar to that of the pristine case. This indicates that the influences of the Fe substitutions on the electronic wave function do not extend too far from the substitution sites. This is further confirmed by the *dI/dV* mapping in Fig. 6(a), lower panel, where the mapping resembles the pristine regions ~1 nm away from the substitution sites. The shapes of the spectra near the substitution sites (S_1 and S_2) exhibit different spectral weight and the spectrum minima biases are shifted from that of the pristine ones. It was reported that the contributions of W in the density of states are mainly around 0.3–0.6 eV above Fermi energy and some below the Fermi energy [98]. This explains that the Fe substitutions at the W sites lower the spectral weight at these energy ranges, which can be seen in Figs. 6(b) and 6(c). Furthermore, by fitting the *dI/dV* spectra near the spectrum minima with a parabolic function, the spectrum minimum biases were determined, as indicated by the inverted triangles in the insets of Figs. 6(b) and 6(c) and summarized in Fig. 6(d). The spectrum minimum bias of the *dI/dV* spectrum taken on the pristine region is determined to be 23.8 ± 0.3 meV. The spectrum minimum biases near the substitution sites are all negative in the range between 0 V and -40 mV, as can be seen in Fig. 6(d). This confirms that the contributions of the electron doping (confirmed by Hall measurements as shown below) are almost identical between the two Fe substitution sites in WTe_2.

The electron doping upon Fe substitutions is further confirmed by Hall measurements. The Hall resistivity $\rho_{xy}(B)$ of the pristine WTe_2 and doped $Fe_{0.011}W_{0.989}Te_2$ are found to show linear field dependence at 200 and at 300 K, as shown in Fig. 7. The Hall coefficients (R_H) extracted by $R_H = d\rho_{xy}/dB$ is found to be -3.01 μΩ cm/T and -1.08 μΩ cm/T at

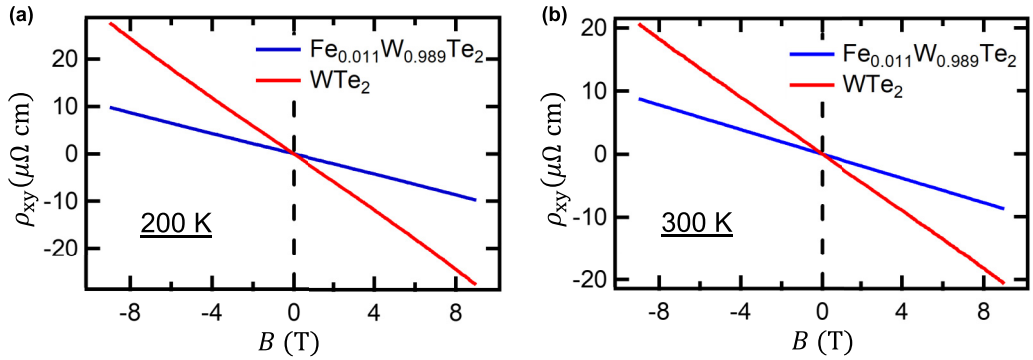

FIG. 7. Hall resistivity measurement of the 1.1 % Fe doped WTe_2 and the pristine WTe_2 at (a) 200 K; and at (b) 300 K.

200 K for pristine WTe_2 and for $Fe_{0.011}W_{0.989}Te_2$, respectively. While for 300 K, the Hall coefficients (R_H) extracted by $R_H = d\rho_{xy}/dB$ is found to be -2.27 μΩ cm/T and -0.97 μΩ cm/T for pristine WTe_2 and for $Fe_{0.011}W_{0.989}Te_2$, respectively. The linear field dependence and negative Hall coefficients suggest the transport is dominated by electron-type carriers. The corresponding charge carrier densities, n, are determined through the single band Hall coefficient, $R_H = \frac{1}{ne}$, where e is the elementary charge. The charge carrier (electron) densities for the pristine WTe_2 and $Fe_{0.011}W_{0.989}Te_2$ are found to be 2.06×10^{20} cm^{-3} and 5.78×10^{20} cm^{-3} at 200 K (2.74×10^{20} cm^{-3} and 6.41×10^{20} cm^{-3} at 300 K), respectively. In another words, the electron density increases with a factor of 2.8 and 2.3 at 200 and 300 K, respectively, upon the Fe doping. This indicates that the Fe dopants provide extra electrons as charge carriers into the WTe_2 crystals, which may play a role in mediating magnetism as discussed above. The small carrier density change revealed by Hall effect, as well as the tiny shift of E_F probed by STM as shown above, indicate light carrier doping, which may be due to the following factors: (1) modification of local environment led to band shift; and (2) WTe_2 is a multiband system with both electron and hole bands at Fermi surfaces. The substitution may cause band dependent scattering that affects Hall effect. On the other hand, the influences of the two types of substitutions on the band structures, which are related to the Weyl points, or their influences on the scattering, which is related to the quasiparticle interference (QPI) results, are still unclear. Further experiments are needed to elucidate these aspects of doping.

IV. SUMMARY

Ferromagnetism is induced due to the 1.1% Fe substitution doping in WTe_2 from the diamagnetic pristine WTe_2. 1.1% Fe doped WTe_2 is also measured with STM/S in details down to the atomic scale. The observed magnetism in undoped WTe_2 is most likely due to the paramagnetic singularity of Weyl points. Likewise, in the case of 1.1% Fe doped WTe_2, FM is most likely due to the coexistence of two effects, (i) paramagnetic singularity for Weyl points, and (ii) Fe substitution doping. At this doping level, WTe_2 grown by CVT technique with I_2 as a transport agent shows substitution doping only. Fe substitutions are responsible for the decrease of interplanar spacing in $Fe_{0.011}W_{0.989}Te_2$. Substitutions of W at the two nonequivalent sites, namely W_1 and W_2 are equally probable, confirmed by the STM and the formation energy calculations. With STS and Hall measurements, Fe substitutions in WTe_2 are found to introduce the electron doping and there are no significant differences in the electron doping between the two doping sites. The results indicate that when substituting Fe into WTe_2, no significant concerns are needed for the precise control of the doping sites on the electron doping behavior. These results exhibit possible coexistence of the Weyl points and the magnetism induced by Fe dopants. Further experiments are needed and encouraged to study the influences of the two substitutions sites on the Weyl points and the QPI behaviors.

ACKNOWLEDGMENTS

D.B. and T.Y.C. acknowledges Wyoming NASA EPSCoR, NASA Grant No. 80NSSC19M0061 and U.S. Department of Energy, Office of Basic Energy Sciences (DE-SC0020074) for STM measurements and analysis. Y.D. and R.Q.R acknowledges U.S. Department of Energy, Office of Basic Energy Sciences (DE-SC0020074) for DFT calculations. W.R.S. and T.Y.C acknowledges the U.S. Department of Energy, Office of Basic Energy Sciences (DE-SC0021281) for STM measurements and analysis. R.B. and J.H. acknowledges U.S. Department of Energy, Office of Basic Energy Sciences (DE-SC0022006) for crystal growth and transport measurements. J.H. and D.U. acknowledges the MonArk NSF Quantum Foundry supported by the National Science Foundation Q-AMASE-i program under NSF Award No. DMR-1906383 for magnetization study using MPMS3 SQUID.

D.B. and W.R.S. performed STM measurements. D.B. analyzed the STM/S data. R.B. prepared the single crystals and performed EDS, XRD, Hall measurements. D.U. performed the magnetization measurements using MPMS. R.B. interpreted the data from magnetization measurement. R.Q.R performed DFT calculation to obtain simulated STM images. T.Y.C., J.H. and Y.D. supervised the project. All authors contributed to the manuscript writing and discussion.

The authors declare no competing financial interests.

[1] M. Z. Hasan and C. L. Kane, *Colloquium:* Topological insulators, Rev. Mod. Phys. **82**, 3045 (2010).

[2] J. E. Moore, The birth of topological insulators, Nature (London) **464**, 194 (2010).

[3] L. Fu and C. L. Kane, Topological insulators with inversion symmetry, Phys. Rev. B **76**, 045302 (2007).

[4] D. Hsieh, D. Qian, L. Wray, Y. Xia, Y. S. Hor, R. J. Cava, and M. Z. Hasan, A topological Dirac insulator in a quantum spin Hall phase, Nature (London) **452**, 970 (2008).

[5] X.-L. Qi, T. L. Hughes, and S.-C. Zhang, Topological field theory of time-reversal invariant insulators, Phys. Rev. B **78**, 195424 (2008).

[6] Y. S. Hor, P. Roushan, H. Beidenkopf, J. Seo, D. Qu, J. G. Checkelsky, L. A. Wray, D. Hsieh, Y. Xia, S.-Y. Xu, D. Qian, M. Z. Hasan, N. P. Ong, A. Yazdani, and R. J. Cava, Development of ferromagnetism in the doped topological insulator $Bi_{2-x}Mn_xTe_3$, Phys. Rev. B **81**, 195203 (2010).

[7] H. Ji, J. M. Allred, N. Ni, J. Tao, M. Neupane, A. Wray, S. Xu, M. Z. Hasan, and R. J. Cava, Bulk intergrowth of a topological insulator with a room-temperature ferromagnet, Phys. Rev. B **85**, 165313 (2012).

[8] A. M. Essin, J. E. Moore, and D. Vanderbilt, Magnetoelectric polarizability and axion electrodynamics in crystalline insulators, Phys. Rev. Lett. **102**, 146805 (2009).

[9] I. Garate and M. Franz, Inverse spin-galvanic effect in the interface between a topological insulator and a ferromagnet, Phys. Rev. Lett. **104**, 146802 (2010).

[10] R. Li, J. Wang, X.-L. Qi, and S.-C. Zhang, Dynamical axion field in topological magnetic insulators, Nat. Phys. **6**, 284 (2010).

[11] R. Yu, W. Zhang, H.-J. Zhang, S.-C. Zhang, X. Dai, and Z. Fang, Quantized anomalous Hall effect in magnetic topological insulators, Science **329**, 61 (2010).

[12] M. Liu, J. Zhang, C.-Z. Chang, Z. Zhang, X. Feng, K. Li, K. He, L. Wang, X. Chen, X. Dai, Z. Fang, Q.-K. Xue, X. Ma, and Y. Wang, Crossover between weak antilocalization and weak localization in a magnetically doped topological insulator, Phys. Rev. Lett. **108**, 036805 (2012).

[13] I. Vobornik, U. Manju, J. Fujii, F. Borgatti, P. Torelli, D. Krizmancic, Y. S. Hor, R. J. Cava, and G. Panaccione, Magnetic proximity effect as a pathway to spintronic applications of topological insulators, Nano Lett. **11**, 4079 (2011).

[14] Y. L. Chen, J.-H. Chu, J. G. Analytis, Z. K. Liu, K. Igarashi, H.-H. Kuo, X. L. Qi, S. K. Mo, R. G. Moore, D. H. Lu, M. Hashimoto, T. Sasagawa, S. C. Zhang, I. R. Fisher, Z. Hussain, and Z. X. Shen, Massive Dirac fermion on the surface of a magnetically doped topological insulator, Science **329**, 659 (2010).

[15] L. A. Wray, S.-Y. Xu, Y. Xia, D. Hsieh, A. V. Fedorov, Y. S. Hor, R. J. Cava, A. Bansil, H. Lin, and M. Z. Hasan, A topological insulator surface under strong Coulomb, magnetic and disorder perturbations, Nat. Phys. **7**, 32 (2011).

[16] A. A. Burkov, Anomalous Hall effect in Weyl metals, Phys. Rev. Lett. **113**, 187202 (2014).

[17] T. Ozawa, Steady-state Hall response and quantum geometry of driven-dissipative lattices, Phys. Rev. B **97**, 041108(R) (2018).

[18] K. Ueda, J. Fujioka, Y. Takahashi, T. Suzuki, S. Ishiwata, Y. Taguchi, M. Kawasaki, and Y. Tokura, Anomalous domain-wall conductance in pyrochlore-type $Nd_2Ir_2O_7$ on the verge of the metal-insulator transition, Phys. Rev. B **89**, 075127 (2014).

[19] X. Wan, A. M. Turner, A. Vishwanath, and S. Y. Savrasov, Topological semimetal and Fermi-arc surface states in the electronic structure of pyrochlore iridates, Phys. Rev. B **83**, 205101 (2011).

[20] G. Xu, H. Weng, Z. Wang, X. Dai, and Z. Fang, Chern semimetal and the quantized anomalous Hall effect in $HgCr_2Se_4$, Phys. Rev. Lett. **107**, 186806 (2011).

[21] D. F. Liu, A. J. Liang, E. K. Liu, Q. N. Xu, Y. W. Li, C. Chen, D. Pei, W. J. Shi, S. K. Mo, P. Dudin, T. Kim, C. Cacho, G. Li, Y. Sun, L. X. Yan, Z. K. Liu, S. Parkin, C. Felser, and Y. L. Chen, Magnetic Weyl semimetal phase in a Kagomé crystal, Science **365**, 1282 (2019).

[22] J. Kübler and C. Felser, Weyl points in the ferromagnetic Heusler compound Co_2MnAl, EPL **114**, 47005 (2016).

[23] Z. Wang, M. G. Vergniory, S. Kushwaha, M. Hirschberger, E. V. Chulkov, A. Ernst, N. P. Ong, R. J. Cava, and B A. Bernevig, Time-reversal-breaking Weyl fermions in magnetic Heusler alloys, Phys. Rev. Lett. **117**, 236401 (2016).

[24] G. Chang, S.-Y. Xu, H. Zheng, B. Singh, C.-H. Hsu, G. Bian, N. Alidoust, I. Belopolski, D. S. Sanchez, S. Zhang, H. Lin, and M. Z. Hasan, Room-temperature magnetic topological Weyl fermion and nodal line semimetal states in half-metallic Heusler Co_2TiX ($X =$ Si, Ge, or Sn), Sci. Rep. **6**, 38839 (2016).

[25] N. P. Armitage, E. J. Mele, and A. Vishwanath, Weyl and Dirac semimetals in three-dimensional solids, Rev. Mod. Phys. **90**, 015001 (2018).

[26] A. A. Burkov and L. Balents, Weyl semimetal in a topological insulator multilayer, Phys. Rev. Lett. **107**, 127205 (2011).

[27] A. A. Zyuzin, S. Wu, and A. A. Burkov, Weyl semimetal with broken time reversal and inversion symmetries, Phys. Rev. B **85**, 165110 (2012).

[28] Q. H. Wang, K. Kalantar-Zadeh, A. Kis, J. N. Coleman, and M. S. Strano, Electronics and optoelectronics of two-dimensional transition metal dichalcogenides, Nat. Nanotechnol. **7**, 699 (2012).

[29] N. F. Mott, Metal-insulator transition, Rev. Mod. Phys. **40**, 677 (1968).

[30] M. Imada, A. Fujimori, and Y. Tokura, Metal-insulator transitions, Rev. Mod. Phys. **70**, 1039 (1998).

[31] D. E. Moncton, J. D. Axe, and F. J. DiSalvo, Neutron scattering study of the charge-density wave transitions in 2H-$TaSe_2$ and 2H-$NbSe_2$, Phys. Rev. B **16**, 801 (1977).

[32] Y. Guo, Y.-F. Zhang, X.-Y. Bao, T.-Z. Han, Z. Tang, L.-X. Zhang, W.-G. Zhu, E. G. Wang, Q. Niu, Z. Q. Qiu, J.-F. Jia, Z.-X. Zhao, and Q.-K. Xue, Superconductivity modulated by quantum size effects, Science **306**, 1915 (2004).

[33] R. C. Morris, R. V. Coleman, and R. Bhandari, Superconductivity and magnetoresistance in $NbSe_2$, Phys. Rev. B **5**, 895 (1972).

[34] P. Samarawickrama, R. Dulal, Z. Fu, U. Erugu, W. Wang, J. Ackerman, B Leonard, J. Tang, T. Chien, and J. Tian, Two-Dimensional 2M-WS_2 nanolayers for superconductivity, ACS Omega. **6**, 2966 (2021).

[35] M. N. Ali, J. Xiong, S. Flynn, J. Tao, Q. D. Gibson, L. M. Schoop, T. Liang, N. Haldolaarachchige, M. Hirschberger, N. P. Ong, and R. J. Cava, Large, nonsaturating magnetoresistance in WTe_2, Nature (London) **514**, 205 (2014).

[36] Y. Tokura and Y. Tomioka, Colossal magnetoresistive manganites, J. Magn. Magn. Mater. **200**, 1 (1999).

[37] Y. Li, H. Wang, L. Xie, Y. Liang, G. Hong, and H. Dai, MoS_2 nanoparticles grown on graphene: An advanced catalyst for the hydrogen evolution reaction, J. Am. Chem. Soc. **133**, 7296 (2011).

[38] L. Rapoport, Y. Bilik, Y. Feldman, M. Homyonfer, S. R. Cohen, and R. Tenne, Hollow nanoparticles of WS_2 as potential solid-state lubricants, Nature (London) **387**, 791 (1997).

[39] A. Ayari, E. Cobas, O. Ogundadegbe, and M. S. Fuhrer, Realization and electrical characterization of ultrathin crystals of layered transition-metal dichalcogenides, J. Appl. Phys. **101**, 014507 (2007).

[40] B Radisavljevic, A. Radenovic, J. Brivio, V. Giacometti, and A. Kis, Single-layer MoS_2 transistors, Nat. Nanotechnol. **6**, 147 (2011).

[41] B Radisavljevic, M. B Whitwick, and A. Kis, Integrated circuits and logic operations based on single-layer MoS_2, ACS Nano. **5**, 9934 (2011).

[42] R. S. Sundaram, M. Engel, A. Lombardo, R. Krupke, A. C. Ferrari, and M. Steiner, Electroluminescence in single layer MoS_2, Nano Lett. **13**, 1416 (2013).

[43] W. Choi, M. Y. Cho, A. Konar, J. H. Lee, G. Cha, S. C. Hong, S. Kim, J. Kim, D. Jena, J. Joo, and S. Kim, High-detectivity multilayer MoS_2 phototransistors with spectral response from ultraviolet to infrared, Adv. Mater. **24**, 5832 (2012).

[44] H.-Y. Chang, S. Yang, J. Lee, L. Tao, W.-S. Hwang, D. Jena, N. Lu, and D. Akinwande, High-performance, highly bendable MoS_2 transistors with high-K dielectrics for flexible low-power systems, ACS Nano. **7**, 5446 (2013).

[45] T. Georgiou, R. Jalil, B D. Belle, L. Britnell, R. V. Gorbachev, S. V. Morozov, Y.-J. Kim, A. Gholinia, S. J. Haigh, O. Makarovsky, L. Eaves, L. A. Ponomarenko, A. K. Geim, K. S. Novoselov, and A. Mishchenko, Vertical field-effect transistor based on graphene–WS_2 heterostructures for flexible and transparent electronics, Nat. Nanotechnol. **8**, 100 (2013).

[46] G.-H. Lee, Y.-J. Yu, X. Cui, N. Petrone, C.-H. Lee, M. S. Choi, D.-Y. Lee, C. Lee, W. J. Yoo, K. Watanabe, T. Taniguchi, C. Nuckolls, P. Kim, and J. Hone, Flexible and transparent MoS_2 field-effect transistors on hexagonal boron nitride-graphene heterostructures, ACS Nano. **7**, 7931 (2013).

[47] X. Qian, J. Liu, L. Fu, and J. Li, Quantum spin Hall effect in two-dimensional transition metal dichalcogenides, Science **346**, 1344 (2014).

[48] Z. Fei, T. Palomaki, S. Wu, W. Zhao, X. Cai, B Sun, P. Nguyen, J. Finney, X. Xu, and D. H. Cobden, Edge conduction in monolayer WTe_2, Nat. Phys. **13**, 677 (2017).

[49] V. Fatemi, S. Wu, Y. Cao, L. Bretheau, Q. D. Gibson, K. Watanabe, T. Taniguchi, R. J. Cava, and P. Jarillo-Herrero, Electrically tunable low-density superconductivity in a monolayer topological insulator, Science **362**, 926 (2018).

[50] Y. Jia, P. Wang, C.-L. Chiu, Z. Song, G. Yu, B Jäck, S. Lei, S. Klemenz, F. A. Cevallos, M. Onyszczak, N. Fishchenko, X. Liu, G. Farahi, F. Xie, Y. Xu, K. Watanabe, T. Taniguchi, B A. Bernevig, R. J. Cava, L. M. Schoop, A. Yazdani, and S. Wu, Evidence for a monolayer excitonic insulator, Nat. Phys. **18**, 87 (2022).

[51] S.-Y. Xu, Q. Ma, H. Shen, V. Fatemi, S. Wu, T.-R. Chang, G. Chang, A. M. M. Valdivia, C.-K. Chan, Q. D. Gibson, J. Zhou, Z. Liu, K. Watanabe, T. Taniguchi, H. Lin, R. J. Cava, L. Fu, N. Gedik, and P. Jarillo-Herrero, Electrically switchable Berry curvature dipole in the monolayer topological insulator WTe_2, Nat. Phys. **14**, 900 (2018).

[52] J. Xiao, Y. Wang, H. Wang, C. D. Pemmaraju, S. Wang, P. Muscher, E. J. Sie, C. M. Nyby, T. P. Devereaux, X. Qian, X. Zhang, and A. M. Lindenberg, Berry curvature memory through electrically driven stacking transitions, Nat. Phys. **16**, 1028 (2020).

[53] A. A. Soluyanov, D. Gresch, Z. Wang, Q. Wu, M. Troyer, X. Dai, and B A. Bernevig, Type-II Weyl semimetals, Nature (London) **527**, 495 (2015).

[54] C.-L. Lin, R. Arafune, R.-Y. Liu, M. Yoshimura, B Feng, K. Kawahara, Z. Ni, E. Minamitani, S. Watanabe, Y. Shi, M. Kawai, T.-C. Chiang, I. Matsuda, and N. Takagi, Visualizing Type-II Weyl points in tungsten ditelluride by quasiparticle interference, ACS Nano. **11**, 11459 (2017).

[55] P. Li, Y. Wen, X. He, Q. Zhang, C. Xia, Z.-M. Yu, S. A. Yang, Z. Zhu, H. N. Alshareef, and X.-X. Zhang, Evidence for topological type-II Weyl semimetal WTe_2, Nat. Commun. **8**, 2150 (2017).

[56] Z.-Y. Jia, Y.-H. Song, X.-B. Li, K. Ran, P. Lu, H.-J. Zheng, X.-Y. Zhu, Z.-Q. Shi, J. Sun, J. Wen, Di. Xing, and S.-C. Li, Direct visualization of a two-dimensional topological insulator in the single-layer $1T' - WTe_2$, Phys. Rev. B **96**, 041108(R) (2017).

[57] S. Tang, C. Zhang, Di. Wong, Z. Pedramrazi, H. Z. Tsai, C. Jia, B Moritz, M. Claassen, H. Ryu, S. Kahn, J. Jiang, H. Yan, M. Hashimoto, D. Lu, R. G. Moore, C. C. Hwang, C. Hwang, Z. Hussain, Y. Chen, M. M. Ugeda, Z. Liu, X. Xie, T. P. Devereaux, M. F. Crommie, S. K. Mo, and Z. X. Shen, Quantum spin Hall state in monolayer 1T'-WTe_2, Nat. Phys. **13**, 683 (2017).

[58] L. Peng, Y. Yuan, G. Li, X. Yang, J. J. Xian, C. J. Yi, Y. G. Shi, and Y. S. Fu, Observation of topological states residing at step edges of WTe_2, Nat. Commun. **8**, 659 (2017).

[59] S. Wu, V. Fatemi, Q. D. Gibson, K. Watanabe, T. Taniguchi, R. J. Cava, and P. Jarillo-Herrero, Observation of the quantum spin Hall effect up to 100 kelvin in a monolayer crystal, Science **359**, 76 (2018).

[60] L. Yang, H. Wu, L. Zhang, W. Zhang, L. Li, T. Kawakami, K. Sugawara, T. Sato, G. Zhang, P. Gao, Y. Muhammad, X. Wen, B. Tao, F. Guo, and H. Chang, Highly tunable near-room temperature ferromagnetism in Cr-Doped layered Td-WTe_2, Adv. Funct. Mater. **31**, 2008116 (2021).

[61] Z. Muhammad, H. Lv, C. Wu, M. Habib, Z. Rehman, R. Khan, S. Chen, X. Wu, and L. Song, Room temperature ferromagnetism in Fe-doped semiconductor ZrS_2 single crystals, Mater. Res. Express. **5**, 046110 (2018).

[62] B Li, T. Xing, M. Zhong, L. Huang, N. Lei, J. Zhang, J. Li, and Z. Wei, A two-dimensional Fe-doped SnS_2 magnetic semiconductor, Nat. Commun. **8**, 1958 (2017).

[63] L. Sun, W. Zhou, Y. Liang, L. Liu, and P. Wu, Magnetic properties in Fe-doped SnS_2: Density functional calculations, Comput. Mater. Sci. **117**, 489 (2016).

[64] Y. C. Cheng, Z. Y. Zhu, W. B. Mi, Z. B. Guo, and U. Schwingenschlögl, Prediction of two-dimensional diluted magnetic semiconductors: Doped monolayer MoS_2 systems, Phys. Rev. B **87**, 100401(R) (2013).

[65] A. Ramasubramaniam and D. Naveh, Mn-doped monolayer MoS_2: An atomically thin dilute magnetic semiconductor, Phys. Rev. B **87**, 195201 (2013).

[66] R. Mishra, W. Zhou, S. J. Pennycook, S. T. Pantelides, and J.-C. Idrobo, Long-range ferromagnetic ordering in manganese-doped two-dimensional dichalcogenides, Phys. Rev. B **88**, 144409 (2013).

[67] I. Horcas, J. M. Gómez-Rodriguez, J. Colchero, J. Gómez-Herrero, and A. M. Baro, WSXM: A software for scanning probe microscopy and a tool for nanotechnology, Rev. Sci. Instrum. **78**, 013705 (2007).

[68] R. A. Vargas−Hernández, Bayesian optimization for calibrating and selecting hybrid-density functional models, J. Phys. Chem. A. **124**, 4053 (2020).

[69] G. Kresse and J. Furthmüller, Efficiency of *ab initio* total energy calculations for metals and semiconductors using a plane-wave basis set, Comput. Mater. Sci. **6**, 15 (1996).

[70] G. Kresse and J. Hafner, *Ab initio* molecular-dynamics simulation of the liquid-metal–amorphous-semiconductor transition in germanium, Phys. Rev. B **49**, 14251 (1994).

[71] P. E. Blöchl, Projector augmented-wave method, Phys. Rev. B **50**, 17953 (1994).

[72] J. P. Perdew, K. Burke, and M. Ernzerhof, Generalized gradient approximation made simple, Phys. Rev. Lett. **77**, 3865 (1996).

[73] S. Grimme, J. Antony, S. Ehrlich, and H. Krieg, A consistent and accurate *ab initio* parametrization of density functional dispersion correction (DFT-D) for the 94 elements H-Pu, J. Chem. Phys. **132**, 154104 (2010).

[74] J. Augustin, V. Eyert, T. Böker, W. Frentrup, H. Dwelk, C. Janowitz, and R. Manzke, Electronic band structure of the layered compound Td-WTe_2, Phys. Rev. B **62**, 10812 (2000).

[75] X.-C. Pan, X. Chen, H. Liu, Y. Feng, Z. Wei, Y. Zhou, Z. Chi, L. Pi, F. Yen, F. Song, X. Wan, Z. Yang, B Wang, G. Wang, and Y. Zhang, Pressure-driven dome-shaped superconductivity and electronic structural evolution in tungsten ditelluride, Nat. Commun. **6**, 7805 (2015).

[76] B E. Brown, The crystal structures of WTe_2 and high-temperature $MoTe_2$, Acta Crystallogr. **20**, 268 (1966).

[77] S. W. Hla, V. Marinkovic, A. Prodan, and I. Musevic, STM/AFM investigations of β-$MoTe_2$, α-$MoTe_2$ and WTe_2, Surf. Sci. **352–354**, 105 (1996).

[78] L. Zhao, H. Deng, I. Korzhovska, Z. Chen, M. Konczykowski, A. Hruban, V. Oganesyan, and L. Krusin-Elbaum, Singular robust room-temperature spin response from topological Dirac fermions, Nat. Mater. **13**, 580 (2014).

[79] R. Singha, A. Pariari, B Satpati, and P. Mandal, Magnetotransport properties and evidence of a topological insulating state in LaSbTe, Phys. Rev. B **96**, 245138 (2017).

[80] A. Pariari and P. Mandal, Coexistence of topological Dirac fermions on the surface and three-dimensional Dirac cone state in the bulk of $ZrTe_5$ single crystal, Sci. Rep. **7**, 40327 (2017).

[81] R. Singha, B. Satpati, and P. Mandal, Fermi surface topology and signature of surface Dirac nodes in LaBi, Sci. Rep. **7**, 6321 (2017).

[82] L. Cai, J. He, Q. Liu, T. Yao, L. Chen, W. Yan, F. Hu, Y. Jiang, Y. Zhao, T. Hu, Z. Sun, and S. Wei, Vacancy-Induced ferromagnetism of MoS_2 nanosheets, J. Am. Chem. Soc. **137**, 2622 (2015).

[83] S. Tongay, J. Zhou, C. Ataca, J. Liu, J. S. Kang, T. S. Matthews, L. You, J. Li, J. C. Grossman, and J. Wu, Broad-range modulation of light emission in two-dimensional semiconductors by molecular physisorption gating, Nano Lett. **13**, 2831 (2013).

[84] M. L. Bortz, F. S. Ohuchi, and B A. Parkinson, An investigation of the growth of Au and Cu on the van der Waals surfaces of $MoTe_2$ and WTe_2, Surf. Sci. **223**, 285 (1989).

[85] Z. Wang, R. Li, C. Su, and K. P. Loh, Intercalated phases of transition metal dichalcogenides, SmartMat. **1**, 1013 (2020).

[86] L. Zhu, Q. Y. Li, Y. Y. Lv, S. Li, X. Y. Zhu, Z. Y. Jia, Y. B Chen, J. Wen, and S. C. Li, Superconductivity in potassium-intercalated Td-WTe_2, Nano Lett. **18**, 6585 (2018).

[87] M. R. Laskar, D. N. Nath, L. Ma, E. W. L. Lee, C. H. Lee, T. Kent, Z. Yang, R. Mishra, M. A. Roldan, J.-C. Idrobo, S. T. Pantelides, S. J. Pennycook, R. C. Myers, Y. Wu, and S. Rajan, p-type doping of MoS_2 thin films using Nb, Appl. Phys. Lett. **104**, 092104 (2014).

[88] K. Dolui, I. Rungger, C. Das Pemmaraju, and S. Sanvito, Possible doping strategies for MoS_2 monolayers: An *ab initio* study, Phys. Rev. B **88**, 075420 (2013).

[89] Y. Gong, Z. Liu, A. R. Lupini, G. Shi, J. Lin, S. Najmaei, Z. Lin, A. L. Elías, A. Berkdemir, G. You, H. Terrones, M. Terrones, R. Vajtai, S. T. Pantelides, S. J. Pennycook, J. Lou, W. Zhou, and P. M. Ajayan, Band gap engineering and layer-by-layer mapping of selenium-doped molybdenum disulfide, Nano Lett. **14**, 442 (2014).

[90] S. Mouri, Y. Miyauchi, and K. Matsuda, Tunable photoluminescence of monolayer MoS_2 via chemical doping, Nano Lett. **13**, 5944 (2013).

[91] L. S. Xie, S. Husremović, O. Gonzalez, I. M. Craig, and D. K. Bediako, Structure and magnetism of iron- and chromium-intercalated niobium and tantalum disulfides, J. Am. Chem. Soc. **144**, 9525 (2022).

[92] Y.-Y. Lv, L. Cao, X. Li, B-B Zhang, K. Wang, Bin Pang, L. Ma, D. Lin, S.-H. Yao, J. Zhou, Y. B Chen, S.-T. Dong, W. Liu, M.-H. Lu, Y. Chen, and Y.-F. Chen, Composition and temperature-dependent phase transition in miscible $Mo_{1-x}W_xTe_2$ single crystals, Sci. Rep. **7**, 44587 (2017).

[93] H. Zhu, R. Addou, Q. Wang, Y. Nie, K. Cho, M. J. Kim, and R. M. Wallace, Surface and interfacial study of atomic layer deposited Al_2O_3 on $MoTe_2$ and WTe_2, Nanotechnology. **31**, 055704 (2020).

[94] H. Kwon, T. Jeong, S. Appalakondaiah, Y. Oh, I. Jeon, H. Min, S. Park, Y. J. Song, E. Hwang, and S. Hwang, Quasiparticle interference and impurity resonances on WTe_2, Nano Res. **13**, 2534 (2020).

[95] H.-Y. Song and J.-T. Lü, Single-site point defects in semimetal WTe_2: A density functional theory study, AIP Adv. **8**, 125323 (2018).

[96] L. Daukiya, M. N. Nair, S. Hajjar-Garreau, F. Vonau, D. Aubel, J. L. Bubendorff, M. Cranney, E. Denys, A. Florentin, G. Reiter, and L. Simon, Highly *n*-doped graphene generated through intercalated terbium atoms, Phys. Rev. B **97**, 035309 (2018).

[97] S. Tiwari, M. L. Van de Put, B Sorée, and W. G. Vandenberghe, Magnetic order and critical temperature of substitutionally doped transition metal dichalcogenide monolayers, npj 2D Mater. Appl. **5**, 54 (2021).

[98] H. Y. Lv, W. J. Lu, D. F. Shao, Y. Liu, S. G. Tan, and Y. P. Sun, Perfect charge compensation in WTe_2 for the extraordinary magnetoresistance: From bulk to monolayer, EPL. **110**, 37004 (2015).